ACS Catalysis

pubs.acs.org/acscatalysis

Research Article

Operando Spectral and Electrochemical Investigation into the Heterophase Stimulated Active Species Transformation in Transition-Metal Sulfides for Efficient Electrocatalytic Oxygen Evolution

Miao Wang, Chung-Li Dong, Yu-Cheng Huang, and Shaohua Shen*

Cite This: *ACS Catal.* 2020, 10, 1855−1864

Read Online

ACCESS | Metrics & More | Article Recommendations | Supporting Information

ABSTRACT: In-depth understanding of electrocatalytically active species transformation during oxygen evolution reaction (OER) is highly guidable to design effective electrocatalysts for water splitting. Herein, cobalt sulfide (CoS_x) nanovesicles decorated with iron sulfide (FeS_x) heterophases were successfully synthesized by using a metal−organic framework precursor through a solvothermal method. The obtained CoS_x/FeS_x exhibited much elevated OER activity as compared to pristine CoS_x and even most previously reported cobalt-based electrocatalysts, with the overpotential of 304 mV at 10 mA cm^{-2} in 1 M KOH. As revealed by operando Raman and X-ray absorption spectroscopy measurements, the electrocatalytically active species transformation in CoS_x nanovesicles could be stimulated by the incorporated FeS_x heterophases due to the increased average valence state of cobalt and lowered coordination of cobalt sites. As a result, the electrocatalytically active cobalt oxyhydroxides could be more easily formed on the catalyst surface during OER and thus contributed to the highly improved performance. This real-time spectral and electrochemical insight into the electrocatalytically active species transformation may guide the rational design of highly efficient electrocatalysts for water splitting from the viewpoint of electronic structure-electrocatalytic activity relationship.

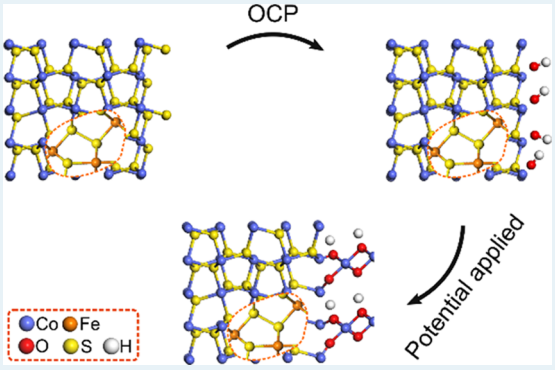

KEYWORDS: *oxygen evolution reaction, cobalt sulfides, operando Raman spectroscopy, operando X-ray absorption spectroscopy, active species transformation*

INTRODUCTION

Electrocatalytic water splitting for hydrogen production has been widely regarded as a promising approach to solve energy and environmental problems.[1,2] However, the current industrialized electrolyzer devices are based on platinum group metals (PGM) with high material cost for proton exchange membrane electrolyzers or PGM-free catalysts with high energy consumption for alkaline electrolyzers.[3,4] Compared with hydrogen evolution reaction with only two electrons involved in one hydrogen molecule production, the four-electron-pathway oxygen evolution reaction (OER) is recognized as the rate-limiting step for water splitting.[5] Therefore, it is critical to develop effective electrocatalysts for high-performance OER, especially those noble-metal-free materials, in consideration of the high cost and scarcity of noble-metal elements on earth.

It is known that applying positive potentials usually causes oxidation of the as-prepared electrocatalysts during the electrochemical OER.[6−8] For example, Smith et al. found that cobalt and nickel oxide catalysts experienced valence state alternation during repeated cyclic voltammetry (CV) measurements, suggesting a quasi-reversible Co^{3+}/Co^{2+} and Ni^{3+}/Ni^{2+} redox process catalyzing OER.[9] Further note that the oxidized species prefer to serve as actual active sites for OER, so that the as-prepared electrocatalysts have been always in situ electrochemically activated on purpose to improve electrocatalytic performances. For example, Zhou et al. first synthesized Ni−Fe disulfide nanosheets through a sulfidation annealing process, which were then treated by an electrochemical oxidation process to obtain the target Ni−Fe disulfide@oxyhydroxide electrocatalyst.[10] With the highly active sites provided by electrochemically formed surface oxyhydroxide layer, the catalyst exhibited an excellent OER performance with the overpotential decreased by 120 mV at the current density of 10 mA cm^{-2} as compared with the noble-metal-based catalyst (RuO_2). For sure, it is necessary to investigate the morphology,

Received: November 29, 2019
Revised: December 31, 2019
Published: January 3, 2020

https://dx.doi.org/10.1021/acscatal.9b05170
ACS Catal. 2020, 10, 1855−1864

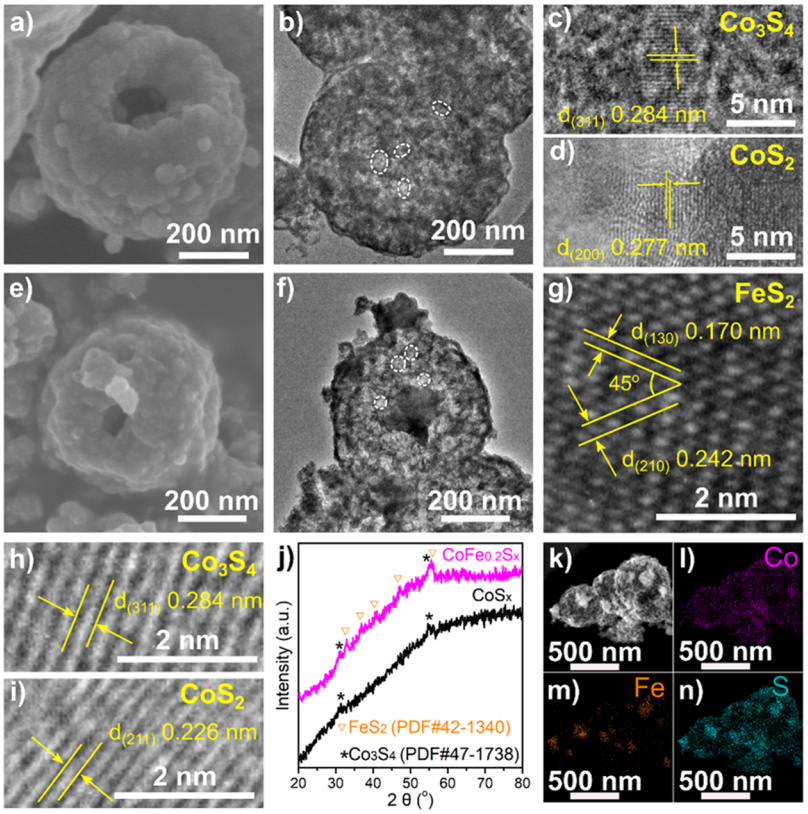

Figure 1. Characteristics of CoS_x: (a) SEM and (b) TEM images, and HRTEM images for (c) Co_3S_4 (#PDF 47-1738) and (d) CoS_2 (#PDF 41-1471). Characteristics of $CoFe_{0.2}S_x$: (e) SEM and (f) TEM images. HRTEM images for (g) FeS_2 (#PDF 42-1340), (h) Co_3S_4 (#PDF 47-1738), and (i) CoS_2 (#PDF 41-1471). (j) XRD patterns. (k) Scanning TEM (STEM) image and EDS elemental mappings of (l) Co, (m) Fe, and (n) S.

structure, and electron configuration of the as-prepared catalyst (the so-called "precatalyst") and their contribution to the electrocatalytic performance. More importantly, exploring the phase transformation during OER can be highly informative to identify the real surface-active species dominating the electrocatalytic activity. However, it is still not easy to obtain the firsthand data of electrocatalysts under real-time reactions, which hinders the deep understanding of reaction mechanisms and the development of superior electrocatalysts for water splitting.

Thanks to the fast progress in experimental tools and devices, it is feasible to realize real-time tracking for reactions by integrating electrochemical measurement systems with spectrometer devices to collect the operando spectra for phase and active species transformation under reactive conditions.[11−14] Cheng et al. adopted a homemade cell for operando Fourier transform (FT) infrared spectroscopy to monitor the phase transformation on NiFe metal−organic frameworks (MOFs) during OER,[15] and successfully detected the surface intermediate superoxide species generated under water oxidation potential, which were crucial for the four-electron-pathway OER. Raman spectroscopy is another powerful tool to provide insightful information on phase and species transformation during electrocatalytic reactions. For example, Louie and Bell confirmed the γ-NiOOH active phase generated on the Ni−Fe oxide film and the conversion process, that the electrochemical species transformed from $Ni(OH)_2$ to NiOOH under the increasing potentials during OER, by collecting a series of operando Raman spectra.[16] Chen and Cai et al. observed structure transformation of $NiCoO_xH_y$ catalysts during OER via operando Raman spectroscopy, which revealed an initial transformation from spinel to a-CoO structure and subsequent conversion to NiOOH-h-CoO_2 under increased potentials.[13] In addition to the techniques above, X-ray absorption spectroscopy (XAS) has been widely used to determine the local geometric and/or electronic structure of materials under the rapid development in synchrotron radiation light sources, which would be then highly attractive for exploring the in situ electrochemical structure and/or phase evolution, especially when combined with electrochemical measurements.[17] For example, as informed from the operando XAS data of cobalt selenides under OER condition,[18] Zhu et al. demonstrated the structural transformation from precatalyst into the real reactive species (i.e., cobalt oxyhydroxides) by revealing the valence states of cobalt under different applied potentials. Su et al. reported NiFe Prussian blue analogue as a promising electrocatalyst for OER in alkaline conditions and elucidated that the reversible potential-dependent deprotonation process ($Ni^{2+}(OH)_2 + xOH^- \rightarrow Ni^{(2+x)+}OOH_{2-x} + xH_2O + xe^-$) contributed to the efficient electrocatalytic performance through operando XAS measurements.[19] Given these encouraging achievements, the operando spectral techniques could be effective to deepen the fundamental understanding of electrocatalytically active phase and/or species evolution during electrochemical reactions, which is expected to guide the design of superior electrocatalysts from the viewpoint of phase and/or electronic structure regulation.

In this work, cobalt sulfide nanovesicles (CoS_x) were synthesized through a solvothermal method from MOF (i.e., ZIF-67). With iron sulfide (FeS_x) heterophase decorated onto CoS_x, the obtained $CoFe_{0.2}S_x$ exhibited much improved OER performance, with overpotential at 10 mA cm^{-2} reduced from

https://dx.doi.org/10.1021/acscatal.9b05170
ACS Catal. 2020, 10, 1855−1864

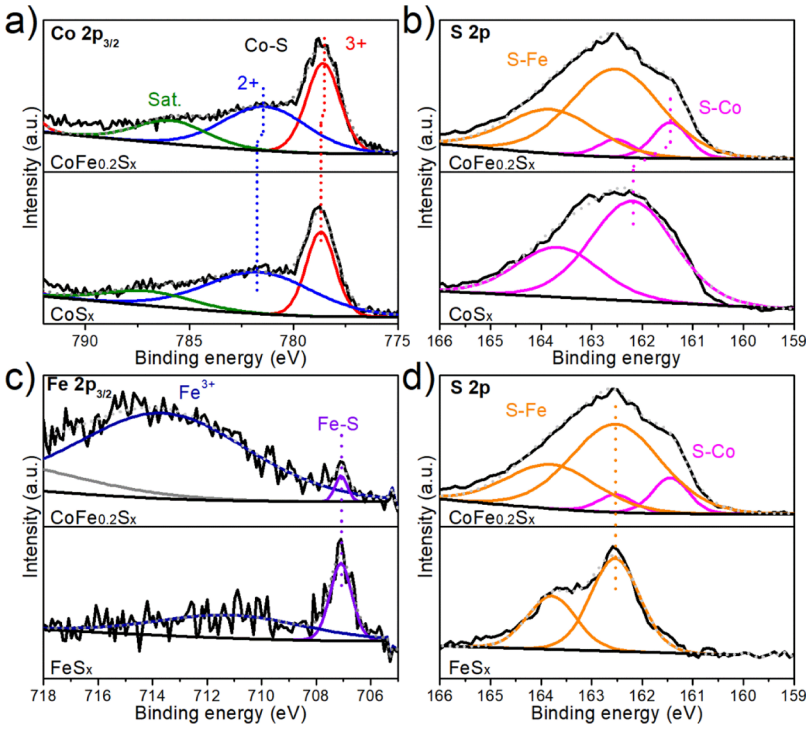

Figure 2. XPS results. (a) Co $2p_{3/2}$ and (b) S 2p XPS results for $CoFe_{0.2}S_x$ and CoS_x. (c) Fe $2p_{3/2}$ and (d) S 2p results for $CoFe_{0.2}S_x$ and FeS_x. FeS_x was synthesized by using a solvothermal method similar to $CoFe_{0.2}S_x$, with $Fe(NO_3)_3{\cdot}9H_2O$ (54.8 mg) but no ZIF-67 was added.

380 to 320 mV in 1 M NaOH (and even 304 mV in 1 M KOH). As revealed by operando spectroscopy technologies (Raman and XAS), cobalt oxyhydroxide (i.e., CoOOH) active species were in situ formed on the surface of CoS_x during the electrochemical process, which dominated the electrocatalytic OER performance. Moreover, the introduced FeS_x heterophases would stimulate the electrochemically active species transformation of CoS_x nanovesicles, which promoted the adsorption of hydroxide ions on cobalt sites and then facilitated the structural transformation for the generation of cobalt oxyhydroxide active species, thus contributing to the remarkable improvement for OER activity. This study may provide an insightful example for real-time tracking of the active species transformation during electrochemical reactions and elucidate the design of high-performance electrocatalysts from the perspective of rational structure regulation.

RESULTS AND DISCUSSION

As derived from hollow ZIF-67 (Figure S1) synthesized according to previous method with some modification,[20] cobalt sulfide (CoS_x) was obtained through a solvothermal process, with the hollow spherical structure of ZIF-67 well inherited (Figure 1a). Interestingly, the obtained CoS_x hollow structure comprises small vesicles (Figures 1b and S2), which are believed to be attributed to the faster outward diffusion of Co ions and the slower inward diffusion of sulfur ions, given the much smaller ionic radius of cobalt ions (74 pm) than that of sulfur ions (184 pm).[21] High-resolution transmission electron microscopy (HRTEM) images (Figures 1c,d and S3) reveal that there are different cobalt sulfide species in CoS_x, as evidenced by the (311) and (200) planes of Co_3S_4 ($d_{(311)}$ = 0.284 nm) and CoS_2 ($d_{(200)}$ = 0.277 nm) phases, respectively. With iron ions introduced in the solvothermal process, the obtained $CoFe_{0.2}S_x$ maintains the hollow spherical morphology (Figure 1e,f), with iron sulfide (e.g., FeS_2) and cobalt sulfide (e.g., Co_3S_4 and CoS_2) species formed, as confirmed by HRTEM images (Figures 1g–i and S4) and X-ray diffraction (XRD) patterns (Figure 1j). The energy dispersive spectroscopy (EDS) elemental mappings of Co, Fe, S, and O elements collected in Figures 1k–n and S5 demonstrate that the FeS_x species are dispersed well in the CoS_x hollow spheres. In addition, the atomic ratio of Fe and Co in $CoFe_{0.2}S_x$ is calculated to be about 0.19 (Figure S6), which coincides well with their initial ratio in precursors. All of the above indicate that the introduced FeS_x phases would not alter the morphology and structure of the hollow spherical CoS_x. Thus, other underlying reasons such as the altered electronic configurations should be explored to reveal their significant effects on electrocatalytic performance.

To probe the possible difference in electronic structures of CoS_x and $CoFe_{0.2}S_x$, X-ray photoelectron spectroscopy (XPS) measurements were carried out. All samples present oxygen peaks (see details in Figure S7), which is almost inevitable in sulfides.[22] As shown in Figure 2a, two Co $2p_{3/2}$ peaks centered at 778.58 and 781.37 eV are observed for $CoFe_{0.2}S_x$, corresponding to Co^{3+} and Co^{2+} in Co–S bonds, respectively. One should note that both peaks present a negative shift to lower binding energies as compared to CoS_x.[21,23] In comparison to the two S 2p peaks observed for CoS_x, there are four peaks for $CoFe_{0.2}S_x$ (Figure 2b), with two peaks at 162.53 and 163.80 eV for Fe–S (S–Fe) bonds and the other two peaks at 161.44 and 162.51 eV for Co–S (S–Co) bonds.[23,24] Moreover, the S 2p peaks related to Co–S bonds in CoS_x exhibit binding energies higher than $CoFe_{0.2}S_x$. Notably, both the binding energy shifts for the Co 2p and S 2p peaks (Figure 2a,b) suggest charge redistribution at Co–S bonds for $CoFe_{0.2}S_x$, as triggered by the introduction of FeS_x heterophases. In addition, the binding energies of Fe 2p and S 2p peaks (Figure 2c,d) for Fe–S (S–Fe) bonds exhibit

https://dx.doi.org/10.1021/acscatal.9b05170
ACS Catal. 2020, 10, 1855–1864

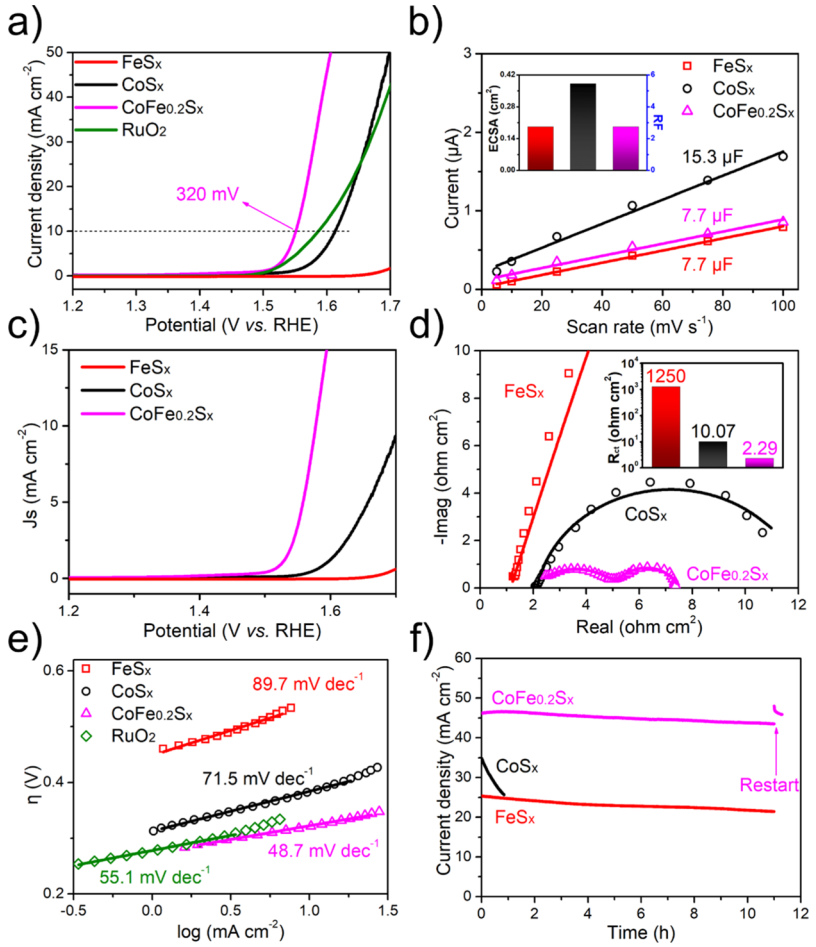

Figure 3. Electrochemical measurements. (a) LSV plots for OER (10 mV s^{-1}, 1 M NaOH). (b) Current-scan rate plots for calculating ECSAs and (c) derived specific current densities. (d) EIS plots. Symbols are measured data; lines are fitted results according to the equal circuits (Figure S11). (e) Tafel plots. (f) OER stability measurement.

negligible shift for $CoFe_{0.2}S_x$ in comparison to the reference iron sulfides (FeS_x),[10,25,26] further evidencing that the introduced FeS_x species exist as heterophases which cause the electronic structure alteration of CoS_x species in $CoFe_{0.2}S_x$. Such heterophases-induced electronic structure alteration may significantly benefit the electrocatalytic OER activity, as revealed in the following part.

The electrocatalytic OER performance was evaluated in a three-electrode system with well-cleaned glassy carbon as the substrate (Figure S8), with linear sweep voltammetry (LSV) plots shown in Figures 3a and S9. It is evident that with the FeS_x heterophase introduced, the obtained sulfides present significantly enhanced OER performances as compared to CoS_x, with the overpotential at 10 mA cm^{-2} reduced to 320 mV for $CoFe_{0.2}S_x$, which is even superior to noble metal catalyst (RuO_2). It is believed that the major active species/phase in a hybrid system can be verified by comparing the respective performance of each component.[27] Note that the pure FeS_x as reference has much poorer OER performance than the pristine CoS_x. Moreover, it was previously reported that cobalt ions could act as major active sites for water oxidation in a binary Co−Fe system.[28] Thus, it can be concluded that the CoS_x phases dominate the OER activity in $CoFe_{0.2}S_x$, and the introduction of FeS_x heterophases triggers the electronic structure evolution of the CoS_x phases (as evidenced by the Co−S bond evolution from the XPS analysis), contributing to the considerable enhancement in OER performance.

Considering the OER occurring at the catalyst/electrolyte interface, the electrochemically active surface area (ECSAs) would be informative to unravel the actual factor which determines the OER activity. As measured by CV methods at different scan rates (Figures S10 and 3b), $CoFe_{0.2}S_x$ possesses ECSA (0.193 cm^2) much smaller than CoS_x (0.383 cm^2), indicating that there are fewer active sites in $CoFe_{0.2}S_x$, possibly due to the partial surface coverage of the CoS_x nanovesicles by FeS_x heterophases (Figure 1k−n). Interestingly, as calculated from LSV and ECSA results, the specific current densities (J_s) imply that $CoFe_{0.2}S_x$ has much higher average activity per reactive site for OER than FeS_x and CoS_x (Figure 3c). Electrochemical impedance spectroscopy (EIS) plots were collected and fitted (Figures 3d and S11) to explore the charge-transfer ability at the catalyst/electrolyte interface that greatly reflected the electrochemical reaction activity. In comparison to FeS_x (1250 Ω cm^2) and pristine CoS_x (10.07 Ω cm^2), $CoFe_{0.2}S_x$ (2.29 Ω cm^2) displays much smaller charge-transfer resistance (R_{ct}), implying the much-accelerated charge-transfer process for electrocatalytic OER. Tafel slopes were further extracted from the LSV results. As shown in Figure 3e, $CoFe_{0.2}S_x$ exhibits a Tafel slope (48.7 mV dec^{-1}) smaller than FeS_x (89.7 mV dec^{-1}), CoS_x (71.5 mV dec^{-1}), and even RuO_2 (55.1 mV dec^{-1}), suggesting the accelerated electrochemical

https://dx.doi.org/10.1021/acscatal.9b05170
ACS Catal. 2020, 10, 1855−1864

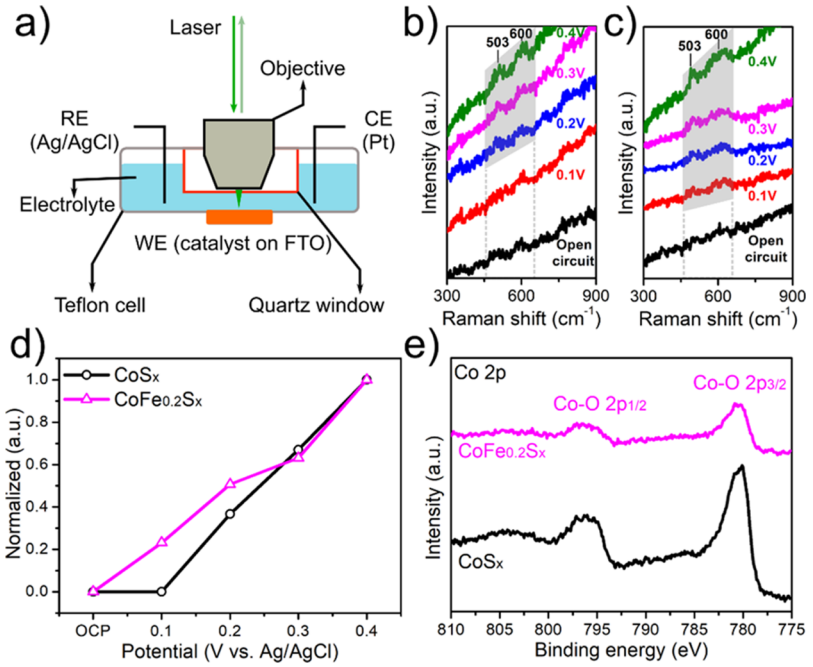

Figure 4. (a) Schematic diagram of the setup, and operando Raman spectra at OCP and different applied potential (vs Ag/AgCl) in 1 M NaOH for (b) CoS_x and (c) $CoFe_{0.2}S_x$. (d) Normalized Raman peak areas at 503 cm^{-1} for CoS_x and $CoFe_{0.2}S_x$. (e) XPS spectrum of Co 2p for CoS_x and $CoFe_{0.2}S_x$ after operando Raman measurement.

reaction kinetics for water oxidation.[29] Given the accelerated interfacial OER reaction kinetics as well evidenced above, it is safe to suggest that the increase in activity of $CoFe_{0.2}S_x$ gives rise to the enhanced OER performance due to the electronic structure evolution of CoS_x phases, as triggered by the introduction of FeS_x heterophases.

Current−time (i−t) plot was also recorded under a fixed bias to evaluate the OER stability (Figure 3f). CoS_x exhibited poor OER stability with a quick attenuation, whereas $CoFe_{0.2}S_x$ exhibited a very slight decrease in current density during the long-time reaction (over 10 h), and the activity revived after removing the bubbles with restarting, indicating that the introduced FeS_x heterophases could not only enhance the activity, but also improve the OER stability. Furthermore, it is encouraging that the obtained $CoFe_{0.2}S_x$ shows excellent OER activity (Figure S12) with overpotential decreasing to 304 mV at 10 mA cm^{-2} in 1 M KOH, which is higher than most of the typical cobalt-based electrocatalysts (Table S1).

It has been demonstrated that for some non-oxide electrocatalysts, a layer of metal oxides/oxyhydroxides would form at the surface and act as the actual active species for electrocatalysis during OER measurement.[30−32] Herein, for $CoFe_{0.2}S_x$, an amorphous layer is formed on the surface, whereas the bulk remains crystallized sulfide phase after the OER stability test (Figure S13). The electrochemically in situ formed oxidative species on the surface is then supposed to serve as the active sites for OER. To elucidate the active species transformation during electrocatalytic OER process, herein, operando Raman spectra were collected by integrating an electrochemical cell with a Raman spectrometer, as shown in Figure 4a. When the samples (CoS_x and $CoFe_{0.2}S_x$) are immersed in the electrolyte, no obvious peaks appear (open circuit in Figure 4b,c). With applied bias increasing, two peaks centered at around 503 and 600 cm^{-1} gradually appear, indicating the generation of cobalt oxyhydroxides under elevated potentials.[12,13,18] It is worth noting that these two peaks can be hardly observed for CoS_x at 0.1 V (Figure 4b), whereas both of them notably appear for $CoFe_{0.2}S_x$ at the same potential (Figure 4c). This difference in potential-dependent phase evolution implies that the phase transformation is thermodynamically easier for $CoFe_{0.2}S_x$ than CoS_x to form cobalt oxyhydroxides under electrochemical reaction conditions (Figure 4d). Furthermore, as demonstrated by the Co 2p XPS (Figure 4e) results, an amorphous oxide layer is formed (Figure S14) after the operando Raman measurements. The observations above indicate that the introduced FeS_x heterophases stimulate the phase transformation of CoS_x and promote the generation of cobalt oxyhydroxides as electrochemical active species, which should be responsible for the improvement of OER performance achieved over $CoFe_{0.2}S_x$.

To further investigate the relationship between OER performance and active species transformation from the viewpoint of electronic structure, operando XAS measurements were also carried out. As revealed in the X-ray absorption near edge structure (XANES) spectra (Figure 5a,b), the inconspicuous prepeaks at around 7710 eV, that serve as a fingerprint feature of metallic character originating from the Co 4sp−Co 3d hybridization, imply the nonmetallic character coinciding with the cobalt sulfide phases for both CoS_x and $CoFe_{0.2}S_x$. The main absorption peaks at around 7725 eV are derived from the electron transition from Co 1s occupied core level to Co 4p unoccupied orbitals.[33] Interestingly, the main peak intensities of CoS_x and $CoFe_{0.2}S_x$ are decreased when the samples are dipped into the electrolyte [open circuit potential (OCP) condition], which are further lowered with the applied potentials increasing. This XANES evolution suggests that the coordination environment of cobalt sulfides changes under different electrochemical conditions.[34] It has been previously evidenced for cobalt phosphides that under alkaline condition, the hydroxide ions would be adsorbed on the surface of cobalt phosphide nanoparticles by replacing the surface phosphorous species.[35] In addition, note that Co−OH species appear for the

https://dx.doi.org/10.1021/acscatal.9b05170
ACS Catal. 2020, 10, 1855−1864

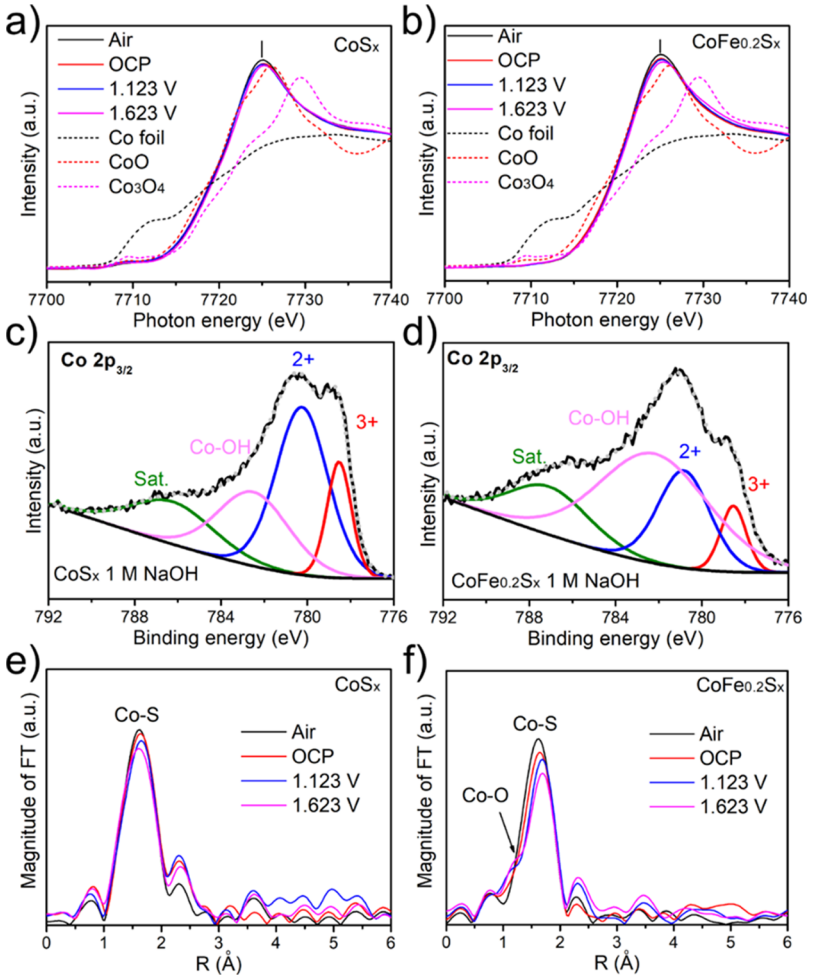

Figure 5. Operando XAS measurements. Operando XANES spectra at the Co K-edge of (a) CoS_x and (b) $CoFe_{0.2}S_x$ in air and at OCP, at 1.123 V, and at 1.623 V (vs RHE) in 1 M NaOH for OER, respectively. XPS results of Co $2p_{3/2}$ for (c) CoS_x and (d) $CoFe_{0.2}S_x$ after being immersed in 1 M NaOH. Corresponding k^3-weighted FT spectra from EXAFS for (e) CoS_x and (f) $CoFe_{0.2}S_x$.

CoS_x and $CoFe_{0.2}S_x$ samples soaked into the electrolyte (Figure 5c,d).[36] Thus, the decrease in main peak intensities with bias applied indicates the continuous dissolution of sulfur ions and adsorption of hydroxide ions. For more detailed comparison, the XANES results of CoS_x and $CoFe_{0.2}S_x$ were overlaid (Figures S15−S18). It is clear that the average valence state of cobalt in $CoFe_{0.2}S_x$ is higher than that of CoS_x in air, at OCP, at 1.123 V, and at 1.623 V, as revealed by the positively shifted absorption edge and enhanced main peak intensity for $CoFe_{0.2}S_x$.[37] It has been reported that the more positively charged sites (i.e., higher average valence state) facilitated the adsorption of hydroxide ions, which benefited the generation of reactive intermediates and thus improved the OER performance.[21,38,39] Moreover, the XPS peak area ratio of Co−OH bond to Co^{2+}/Co^{3+} is higher for $CoFe_{0.2}S_x$ (1.80) than CoS_x (0.46) (Figure 5c,d), indicating that more hydroxide ions are adsorbed at Co sites for $CoFe_{0.2}S_x$ when immersed in the electrolyte. Hence, the increase in the average valence state of cobalt for $CoFe_{0.2}S_x$ is believed to promote the generation of cobalt oxyhydroxides (as revealed in operando Raman spectra in Figure 4) acting as active species during OER measurement.

To reveal the coordination environments of Co sites during OER, the FT of extended X-ray absorption fine structure (EXAFS) spectra was conducted for CoS_x (Figure 5e) and $CoFe_{0.2}S_x$ (Figure 5f). The peaks centered at around 1.6 Å, attributed to the Co−S bonds, decrease successively for both CoS_x and $CoFe_{0.2}S_x$ in air, at OCP, at 1.123 V, and at 1.623 V. This suggests that the amount of sulfur atoms coordinating with cobalt atoms gets decreased because of the sulfur dissolution along with the reaction proceeding. Interestingly, a new peak at around 1.4 Å, representing the Co−O bond, arises at the potential of 1.123 V and continues to increase at 1.623 V for $CoFe_{0.2}S_x$ (Figure 5f), whereas the similar evolution can be hardly observed for CoS_x (Figure 5e).[40] This result indicates that it is easier for $CoFe_{0.2}S_x$ to generate Co−O species than CoS_x, as also evidenced by the operando Raman spectra (Figure 4). In addition, it has been previously demonstrated that coordinatively unsaturated cobalt ions acted as active sites to catalyze OER with the open sites for reactant adsorption.[41,42] Then, it is reasonable that the lower-coordinated cobalt atoms in $CoFe_{0.2}S_x$ than those in CoS_x (Figure S15b) should assist hydroxide ions to be adsorbed on the surface cobalt sites in $CoFe_{0.2}S_x$ and then facilitate the subsequent reaction process.

For a more explicit presentation, the evolution of main peak intensities and magnitudes of FT under various conditions were well-concluded in Figure 6a. It is demonstrated that the increased positive charges at cobalt sites and the lower-coordinated cobalt atoms for $CoFe_{0.2}S_x$ lead to facilitated

https://dx.doi.org/10.1021/acscatal.9b05170
ACS Catal. 2020, 10, 1855−1864

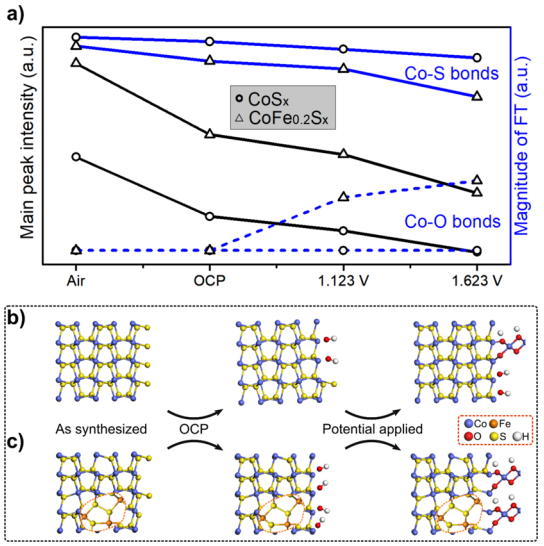

Figure 6. (a) Changes of the main peak intensity in XANES (black solid lines) and the magnitude of FT for Co−S bonds (blue solid lines) and Co−O bonds (blue dashed lines) under different conditions. CoS_x is marked by circles; $CoFe_{0.2}S_x$ is marked by triangles. A typical atomic structure illustration for in situ surface transformation of cobalt species in (b) CoS_x and (c) $CoFe_{0.2}S_x$ under different conditions, with balls for Co (blue), Fe (orange), O (red), S (yellow), and H (gray). The area bordered by orange dashed lines represents a typical atomic structure of FeS_x.

formation of cobalt oxyhydroxides during the electrochemical process, as compared with CoS_x. Based on the operando spectral analyses above, a surface electrochemical transformation mechanism for the improved OER performance can be proposed. When the as-synthesized CoS_x is immersed in the aqueous electrolyte (at OCP) containing sufficient hydroxide ions, some Co−S bonds at the surface of CoS_x are broken with sulfur ligands dissolved in the electrolyte, whereas some hydroxide ions in the electrolyte are adsorbed onto the Co sites (Figure 6b), which has been verified by the XAS and XPS results in Figure 5. Consequently, with positive potential applied for OER, hydroxide ions are further adsorbed onto Co sites; simultaneously, cobalt oxyhydroxides are generated to form a sulfide/oxyhydroxide heterostructure.[43] Comparatively, the introduction of FeS_x heterophases causes the Co sites to be more positively charged with decreased sulfur ligands (as discussed in Figures 5 and S15), thus resulting in the promoted adsorption of hydroxide ions for $CoFe_{0.2}S_x$ immersed in the electrolyte (Figure 6c). Subsequently, as compared to CoS_x, when positive potential is applied, more cobalt oxyhydroxides are formed and serve as reactive sites for OER, which endows the significantly enhanced electrocatalytic performance for $CoFe_{0.2}S_x$.

CONCLUSIONS

Cobalt sulfides decorated with iron sulfides were synthesized through a solvothermal method derived from ZIF-67, exhibiting promoted OER performance with overpotential of 304 mV at 10 mA cm^{-2} in 1 M KOH and a long-time stability. It was revealed that cobalt oxyhydroxide active species were formed on cobalt sulfide surface during the OER process, which dominated the electrocatalytic performance. Moreover, the introduced FeS_x heterophases stimulated the active species transformation of cobalt sulfides for the improved OER performance: the higher average valence state of cobalt sites and the decreased sulfur ligands promoted the adsorption of hydroxide ions on cobalt sites, which facilitated the in situ electrochemical generation of cobalt oxyhydroxide active species. This work uses operando spectroscopy techniques to explore the surface-active species transformation during the electrocatalytic process, which may provide informative guidance for the deep understanding of the electrocatalysis mechanisms and the rational design of highly efficient electrocatalysts for water splitting.

EXPERIMENTAL SECTION

Materials. Cobalt sulfate ($CoSO_4·7H_2O$, analytical pure), 2-methylimidazole (99%), methanol (analytical pure), ethanol (analytical), thioacetamide (TAA, analytical pure), ferric nitrate [$Fe(NO_3)_3·9H_2O$, analytical pure], sodium hydroxide (NaOH, analytical pure), potassium hydroxide (KOH, analytical pure), and RuO_2 (99%) were purchased from Sinopharm Chemical Reagent Co., Ltd (SCRC). Ultrapure water (18.25 MΩ cm) was used for the aqueous solutions.

Synthesis of Hollow ZIF-67. $CoSO_4·7H_2O$ (2342.5 mg) and 2-methylimidazole (6568 mg) were dissolved in methanol (200 mL) at room temperature, respectively. Then, the two solutions were mixed and stirred for 1 h at 1000 rpm. Purple powders were collected after several wash-centrifugation cycles by methanol and subsequent drying at 60 °C for 6 h.

Synthesis of CoS_x. ZIF-67 (30 mg) and TAA (120 mg) were mixed in ethanol (60 mL), treated by ultrasonication for 10 min, and then put into a sealed autoclave under 180 °C for 12 h. After cooled naturally, the collected dark precipitation was washed by ethanol several times and finally dried at 60 °C, and marked as CoS_x.

Synthesis of $CoFe_{0.2}S_x$. $CoFe_{0.2}S_x$ was synthesized by a solvothermal process similar to CoS_x, with $Fe(NO_3)_3·9H_2O$ (mole ratio of Fe to Co set at 0.2) added into ethanol before ultrasonic treatment.

Characterizations. Field emission scanning electron microscopy (FE-SEM, JEOL JSM-7800F) and transmission electron microscopy (TEM, G2F30 FEI) were used for morphology and structure characterization. Energy dispersive X-ray detectors (OXFORD MAX-80) were used for elemental analysis. XPS measurements were conducted on a Kratos spectrometer (AXIS Ultra DLD) with monochromatic Al Kα radiation ($h\nu$ = 1486.69 eV) and a concentric hemispherical analyzer, and the calibration of binding energy was performed with the C 1s line (284.8 eV) in the samples. Raman scattering was performed with an argon ion laser at 20 mW (514.5 nm, Jobin Yvon LabRAM HR800). XRD patterns were collected by X-ray diffractometer (PANalytical, Cu Kα, λ = 0.15406 nm). The synchrotron XAS data were obtained at TPS44A at the National Synchrotron Radiation Research Center (NSRRC), Taiwan.

Electrochemical Test. The sample (4 mg) was dispersed in a mixed solution of ultrapure water (1000 μL), ethanol (1000 μL), and Nafion (10 wt %, 40 μL). After being treated by ultrasonication for 30 min, the formed ink (5 μL) was dropped on the polished glassy carbon electrode (GCE) and dried at room temperature to serve as the working electrode with a final mass loading of 0.14 mg cm^{-2}. The electrochemical measurements were carried out in a three-electrode cell connected with an electrochemical workstation (CHI 760D), in which Hg/HgO (1 M NaOH, CHI 152) and Pt wire (CHI 115) served as the reference electrode and counter electrode,

https://dx.doi.org/10.1021/acscatal.9b05170
ACS Catal. 2020, 10, 1855−1864

respectively. NaOH aqueous solution (1 M) saturated with O_2 was used as the electrolyte. Before the test, the sample was swept by the CV method for several cycles between −0.1 and 0.7 V (vs Hg/HgO) until the current became stabilized. For evaluating OER performance, LSV measurements were conducted with a scan rate of 10 mV s^{-1}. Tafel plots were calculated from LSV results according to the equation: $\eta = a + b \log|j|$, in which η is the overpotential, a is the intercept, b is the Tafel slope, and $|j|$ is the absolute value of current density. EIS measurements were carried out with a frequency range of 0.1 Hz to 100 kHz at a controlled potential of 0.65 V (vs Hg/HgO). CVs at scan rates from 5 to 100 mV s^{-1} between −0.05 and 0.05 V (vs Hg/HgO) were carried out, then the double layer capacitances (C_{dl}) could be calculated as the quotient: $((J_a - J_c)/2)/\nu$, where J_a and J_c were the positive and negative scan currents at 0 V (vs Hg/HgO), respectively. Thus, the ECSA could be calculated by dividing C_{dl} by a specific capacitance (C_s), where C_s was assumed to be 40 μF cm^{-2} in 1 M NaOH. Roughness factor (RF) was obtained by dividing ECSA by the geometric area of the GCE, and specific current density (J_s) was the quotient of geometric current density divided by RF. The measurement for stability (i.e., i−t test) was conducted in 1 M NaOH under a fixed bias with a two-electrode configuration in a cell separated by a Nafion 117 membrane. The catalyst was dropped on a cleaned nickel foam with a mass loading of 0.67 mg cm^{-2} as the working electrode, whereas a Pt plate (1 × 1 cm) served as the counter electrode. The potentials were calibrated to the reversible hydrogen evolution (RHE) electrode by the Nernst equation: E(vs RHE) = E(vs Hg/HgO) + 0.924 V.

Operando Raman Spectra. The operando Raman spectra were collected by combination of a Raman spectrometer and an electrochemical workstation. For Raman spectra collection, the laser was set at 20 mW and at 514.5 nm, with lens of 10×/0.25, attenuation of D1, and collecting time of 500 s. A three-electrode configuration was adopted in a commercial Teflon cell with a quartz window (031, Gaoss Union). The catalyst was dropped on a conductive FTO glass as the working electrode, whereas a Pt wire and Ag/AgCl (saturated KCl) acted as the counter electrode and reference electrode, respectively. NaOH (1 M) was used as the electrolyte. The Raman spectra were collected when various potentials were maintained.

Operando XAS Measurements. The measurements were performed in a home-made Teflon cell with a window sealed by Kapton tape by a three-electrode configuration in 1 M NaOH, with a Pt wire serving as the counter electrode, Ag/AgCl (saturated KCl) as the reference electrode, and the sample loaded on carbon paper as the working electrode. X-ray was allowed to transmit through the tape and the carbon paper; thus, the signal could be collected in the transmission mode. The XAS spectra were recorded in order of sample in air, at OCP, at 0.1 V (vs Ag/AgCl), and at 0.6 V (vs Ag/AgCl). The potentials were calibrated to the RHE electrode by the Nernst equation: E (vs RHE) = E (vs Ag/AgCl) + 1.023 V.

■ ASSOCIATED CONTENT

Supporting Information

The Supporting Information is available free of charge at https://pubs.acs.org/doi/10.1021/acscatal.9b05170.

SEM, TEM, EDS mapping images, XRD patterns, LSV plots, CV plots, XANES and EXAFS results, and comparison of OER performances of some reported cobalt-based catalysts supported on GCE (PDF)

■ AUTHOR INFORMATION

Corresponding Author

Shaohua Shen − *Xi'an Jiaotong University, Shaanxi, China;* orcid.org/0000-0001-8536-7386; Email: shshen_xjtu@mail.xjtu.edu.cn

Other Authors

Miao Wang − *Xi'an Jiaotong University, Shaanxi, China*

Chung-Li Dong − *Tamkang University, New Taipei City, Taiwan;* orcid.org/0000-0002-4289-4677

Yu-Cheng Huang − *Tamkang University, New Taipei City, Taiwan, and National Chiao Tung University, Hsinchu, Taiwan*

Complete contact information is available at: https://pubs.acs.org/10.1021/acscatal.9b05170

Author Contributions

The article was written through contributions of all authors. All authors have given approval to the final version of the article.

Notes

The authors declare no competing financial interest.

■ ACKNOWLEDGMENTS

The authors gratefully acknowledge the financial support from the National Natural Science Foundation of China (nos. 51961165103, 51672210) and the National Key Research and Development Program of China (2018YFB1502003, 2017YFE0193900). S.S. is supported by the National Program for Support of Top-notch Young Professionals. The authors also appreciate the help of Zhidan Diao for technical assistance.

■ REFERENCES

(1) Yan, H.; Xie, Y.; Wu, A.; Cai, Z.; Wang, L.; Tian, C.; Zhang, X.; Fu, H. Anion-Modulated HER and OER Activities of 3D Ni-V-Based Interstitial Compound Heterojunctions for High-Efficiency and Stable Overall Water Splitting. *Adv. Mater.* **2019**, *31*, 1901174.

(2) Li, A.; Sun, Y.; Yao, T.; Han, H. Earth-Abundant Transition-Metal-Based Electrocatalysts for Water Electrolysis to Produce Renewable Hydrogen. *Chem.—Eur J.* **2018**, *24*, 18334−18355.

(3) Abbasi, R.; Setzler, B. P.; Lin, S.; Wang, J.; Zhao, Y.; Xu, H.; Pivovar, B.; Tian, B.; Chen, X.; Wu, G.; Yan, Y. A Roadmap to Low-Cost Hydrogen with Hydroxide Exchange Membrane Electrolyzers. *Adv. Mater.* **2019**, *31*, 1805876.

(4) Zhang, X.; Dong, C. L.; Diao, Z.; Lu, Y. R.; Shen, S. Identifying the Crystal and Electronic Structure Evolution in Tri-component Transition Metal Oxide Nanosheets for Efficient Electrocatalytic Oxygen Evolution. *EcoMat* **2019**, *1*, No. e12005.

(5) Wang, C.; Yang, H.; Zhang, Y.; Wang, Q. NiFe Alloy Nanoparticle with hcp Crystal Structure Stimulates Superior Oxygen Evolution Reaction Electrocatalytic Activity. *Angew. Chem., Int. Ed.* **2019**, *58*, 6099−6103.

(6) Wang, M.; Dong, C.-L.; Huang, Y.-C.; Li, Y.; Shen, S. Electronic Structure Evolution in Tricomponent Metal Phosphides with Reduced Activation Energy for Efficient Electrocatalytic Oxygen Evolution. *Small* **2018**, *14*, 1801756.

(7) Walter, C.; Menezes, P. W.; Orthmann, S.; Schuch, J.; Connor, P.; Kaiser, B.; Lerch, M.; Driess, M. A Molecular Approach to Manganese Nitride Acting as a High Performance Electrocatalyst in the Oxygen Evolution Reaction. *Angew. Chem., Int. Ed.* **2018**, *57*, 698−702.

(8) Li, H.; Li, Q.; Wen, P.; Williams, T. B.; Adhikari, S.; Dun, C.; Lu, C.; Itanze, D.; Jiang, L.; Carroll, D. L.; Donati, G. L.; Lundin, P. M.; Qiu, Y.; Geyer, S. M. Colloidal Cobalt Phosphide Nanocrystals as Trifunctional Electrocatalysts for Overall Water Splitting Powered by a Zinc-Air Battery. *Adv. Mater.* **2018**, *30*, 1705796.
(9) Smith, R. D. L.; Prévot, M. S.; Fagan, R. D.; Trudel, S.; Berlinguette, C. P. Water Oxidation Catalysis: Electrocatalytic Response to Metal Stoichiometry in Amorphous Metal Oxide Films Containing Iron, Cobalt, and Nickel. *J. Am. Chem. Soc.* **2013**, *135*, 11580−11586.
(10) Zhou, M.; Weng, Q.; Zhang, X.; Wang, X.; Xue, Y.; Zeng, X.; Bando, Y.; Golberg, D. In Situ Electrochemical Formation of Core-Shell Nickel-Iron Disulfide and Oxyhydroxide Heterostructured Catalysts for a Stable Oxygen Evolution Reaction and the Associated Mechanisms. *J. Mater. Chem. A* **2017**, *5*, 4335−4342.
(11) Dong, C.-L.; Vayssieres, L. In Situ/Operando X-ray Spectroscopies for Advanced Investigation of Energy Materials. *Chem.—Eur J.* **2018**, *24*, 18356−18373.
(12) Yeo, B. S.; Bell, A. T. Enhanced Activity of Gold-Supported Cobalt Oxide for the Electrochemical Evolution of Oxygen. *J. Am. Chem. Soc.* **2011**, *133*, 5587−5593.
(13) Chen, Z.; Cai, L.; Yang, X.; Kronawitter, C.; Guo, L.; Shen, S.; Koel, B. E. Reversible Structural Evolution of $NiCoO_xH_y$ during the Oxygen Evolution Reaction and Identification of the Catalytically Active Phase. *ACS Catal.* **2018**, *8*, 1238−1247.
(14) Ryu, J.; Jung, N.; Jang, J. H.; Kim, H.-J.; Yoo, S. J. J. In Situ Transformation of Hydrogen-Evolving CoP Nanoparticles: Toward Efficient Oxygen Evolution Catalysts Bearing Dispersed Morphologies with Co-oxo/hydroxo Molecular Units. *ACS Catal.* **2015**, *5*, 4066−4074.
(15) Cheng, W.; Zhao, X.; Su, H.; Tang, F.; Che, W.; Zhang, H.; Liu, Q. Lattice-Strained Metal-Organic-Framework Arrays for Bifunctional Oxygen Electrocatalysis. *Nat. Energy* **2019**, *4*, 115−122.
(16) Louie, M. W.; Bell, A. T. An Investigation of Thin-Film Ni-Fe Oxide Catalysts for the Electrochemical Evolution of Oxygen. *J. Am. Chem. Soc.* **2013**, *135*, 12329−12337.
(17) Wang, M.; Árnadóttir, L.; Xu, Z. J.; Feng, Z. In Situ X-ray Absorption Spectroscopy Studies of Nanoscale Electrocatalysts. *Nano-Micro Lett.* **2019**, *11*, 47.
(18) Zhu, Y.; Chen, H.-C.; Hsu, C.-S.; Lin, T.-S.; Chang, C.-J.; Chang, S.-C.; Tsai, L.-D.; Chen, H. M. *ACS Energy Lett.* **2019**, *4*, 987−994.
(19) Su, X.; Wang, Y.; Zhou, J.; Gu, S.; Li, J.; Zhang, S. Operando Spectroscopic Identification of Active Sites in NiFe Prussian Blue Analogues as Electrocatalysts: Activation of Oxygen Atoms for Oxygen Evolution Reaction. *J. Am. Chem. Soc.* **2018**, *140*, 11286−11292.
(20) Zeng, P.; Li, J.; Ye, M.; Zhuo, K.; Fang, Z. In Situ Formation of Co_9S_8/N-C Hollow Nanospheres by Pyrolysis and Sulfurization of ZIF-67 for High-Performance Lithium-Ion Batteries. *Chem.—Eur J.* **2017**, *23*, 9517−9524.
(21) Dai, Z.; Geng, H.; Wang, J.; Luo, Y.; Li, B.; Zong, Y.; Yang, J.; Guo, Y.; Zheng, Y.; Wang, X.; Yan, Q. Hexagonal-Phase Cobalt Monophosphosulfide for Highly Efficient Overall Water Splitting. *ACS Nano* **2017**, *11*, 11031−11040.
(22) Fan, K.; Zou, H.; Lu, Y.; Chen, H.; Li, F.; Liu, J.; Sun, L.; Tong, L.; Toney, M. F.; Sui, M.; Yu, J. Direct Observation of Structural Evolution of Metal Chalcogenide in Electrocatalytic Water Oxidation. *ACS Nano* **2018**, *12*, 12369−12379.
(23) Wu, L.-L.; Wang, Q.-S.; Li, J.; Long, Y.; Liu, Y.; Song, S.-Y.; Zhang, H.-J. Co_9S_8 Nanoparticles-Embedded N/S-Codoped Carbon Nanofibers Derived from Metal-Organic Framework-Wrapped CdS Nanowires for Efficient Oxygen Evolution Reaction. *Small* **2018**, *14*, 1704035.
(24) Ganesan, P.; Prabu, M.; Sanetuntikul, J.; Shanmugam, S. Cobalt Sulfide Nanoparticles Grown on Nitrogen and Sulfur Codoped Graphene Oxide: An Efficient Electrocatalyst for Oxygen Reduction and Evolution Reactions. *ACS Catal.* **2015**, *5*, 3625−3637.
(25) Miao, R.; Dutta, B.; Sahoo, S.; He, J.; Zhong, W.; Cetegen, S. A.; Jiang, T.; Alpay, S. P.; Suib, S. L. Mesoporous Iron Sulfide for Highly Efficient Electrocatalytic Hydrogen Evolution. *J. Am. Chem. Soc.* **2017**, *139*, 13604−13607.
(26) Piontek, S.; Andronescu, C.; Zaichenko, A.; Konkena, B.; Junge Puring, K.; Marler, B.; Antoni, H.; Sinev, I.; Muhler, M.; Mollenhauer, D.; Roldan Cuenya, B.; Schuhmann, W.; Apfel, U.-P. Influence of the Fe:Ni Ratio and Reaction Temperature on the Efficiency of $(Fe_xNi_{1-x})_9S_8$ Electrocatalysts Applied in the Hydrogen Evolution Reaction. *ACS Catal.* **2018**, *8*, 987−996.
(27) Gu, J.; Hsu, C.-S.; Bai, L.; Chen, H. M.; Hu, X. Atomically Dispersed Fe^{3+} Sites Catalyze Efficient CO_2 Electroreduction to CO. *Science* **2019**, *364*, 1091−1094.
(28) Hung, S.-F.; Chan, Y.-T.; Chang, C.-C.; Tsai, M.-K.; Liao, Y.-F.; Hiraoka, N.; Hsu, C.-S.; Chen, H. M. Identification of Stabilizing High-Valent Active Sites by Operando High-Energy Resolution Fluorescence-Detected X - ray Absorption Spectroscopy for High-Efficiency Water Oxidation. *J. Am. Chem. Soc.* **2018**, *140*, 17263−17270.
(29) Wang, M.; Dong, C.-L.; Huang, Y.-C.; Shen, S. Bifunctional Cobalt Phosphide Nanoparticles with Convertible Surface Structure for Efficient Electrocatalytic Water Splitting in Alkaline Solution. *J. Catal.* **2019**, *371*, 262−269.
(30) Li, H.; Guo, Z.; Wang, X. Atomic-Layer-Deposited Ultrathin Co_9S_8 On Carbon Nanotubes: an Efficient Bifunctional Electrocatalyst for Oxygen Evolution/Reduction Reactions and Rechargeable Zn-air Batteries. *J. Mater. Chem. A* **2017**, *5*, 21353−21361.
(31) Wu, Y.; Liu, Y.; Li, G.-D.; Zou, X.; Lian, X.; Wang, D.; Sun, L.; Asefa, T.; Zou, X. Efficient Electrocatalysis of Overall Water Splitting by Ultrasmall $Ni_xCo_{3-x}S_4$ Coupled Ni_3S_2 Nanosheet Arrays. *Nano Energy* **2017**, *35*, 161−170.
(32) Konkena, B.; Masa, J.; Botz, A. J. R.; Sinev, I.; Xia, W.; Koßmann, J.; Drautz, R.; Muhler, M.; Schuhmann, W. Metallic $NiPS_3$@NiOOH Core−Shell Heterostructures as Highly Efficient and Stable Electrocatalyst for the Oxygen Evolution Reaction. *ACS Catal.* **2017**, *7*, 229−237.
(33) Kim, S. J.; Lee, Y.; Lee, D. K.; Lee, J. W.; Kang, J. K. Efficient Co-Fe Layered Double Hydroxide Photocatalysts for Water Oxidation Under Visible Light. *J. Mater. Chem. A* **2014**, *2*, 4136−4139.
(34) Chen, D.; Dong, C.-L.; Zou, Y.; Su, D.; Huang, Y.-C.; Tao, L.; Dou, S.; Shen, S.; Wang, S. In Situ Evolution of Highly Dispersed Amorphous CoO_x Clusters for Oxygen Evolution Reaction. *Nanoscale* **2017**, *9*, 11969.
(35) Wu, Z.; Gan, Q.; Li, X.; Zhong, Y.; Wang, H. Elucidating Surface Restructuring-Induced Catalytic Reactivity of Cobalt Phosphide Nanoparticles under Electrochemical Conditions. *J. Phys. Chem. C* **2018**, *122*, 2848−2853.
(36) Tan, B. J.; Klabunde, K. J.; Sherwood, P. M. A. XPS Studies of Solvated Metal Atom Dispersed Catalysts. Evidence for Layered Cobalt-Manganese Particles on Alumina and Silica. *J. Am. Chem. Soc.* **1991**, *113*, 855−861.
(37) Wang, H.-Y.; Hung, S.-F.; Chen, H.-Y.; Chan, T.-S.; Chen, H. M.; Liu, B. Operando Identification of Geometrical-Site-Dependent Water Oxidation Activity of Spinel Co_3O_4. *J. Am. Chem. Soc.* **2016**, *138*, 36−39.
(38) Gadipelli, S.; Zhao, T.; Shevlin, S. A.; Guo, Z. Switching Effective Oxygen Reduction and Evolution Performance by Controlled Graphitization of a Cobalt-Nitrogen-Carbon Framework System. *Energy Environ. Sci.* **2016**, *9*, 1661−1667.
(39) Zhuang, L.; Ge, L.; Yang, Y.; Li, M.; Jia, Y.; Yao, X.; Zhu, Z. Ultrathin Iron-Cobalt Oxide Nanosheets with Abundant Oxygen Vacancies for the Oxygen Evolution Reaction. *Adv. Mater.* **2017**, *29*, 1606793.
(40) Dou, S.; Dong, C.-L.; Hu, Z.; Huang, Y.-C.; Chen, J.-L.; Tao, L.; Yan, D.; Chen, D.; Shen, S.; Chou, S.; Wang, S. Atomic-Scale CoO_x Species in Metal-Organic Frameworks for Oxygen Evolution Reaction. *Adv. Funct. Mater.* **2017**, *27*, 1702546.
(41) Zhao, S.; Wang, Y.; Dong, J.; He, C.-T.; Yin, H.; An, P.; Zhao, K.; Zhang, X.; Gao, C.; Zhang, L.; Lv, J.; Wang, J.; Zhang, J.; Khattak,

https://dx.doi.org/10.1021/acscatal.9b05170
ACS Catal. 2020, 10, 1855−1864

A. M.; Khan, N. A.; Wei, Z.; Zhang, J.; Liu, S.; Zhao, H.; Tang, Z. Ultrathin Metal-Organic Framework Nanosheets for Electrocatalytic Oxygen Evolution. *Nat. Energy* **2016**, *1*, 16184.
(42) Tao, L.; Lin, C.-Y.; Dou, S.; Feng, S.; Chen, D.; Liu, D.; Huo, J.; Xia, Z.; Wang, S. Creating Coordinatively Unsaturated Metal Sites in Metal-Organic-Frameworks as Efficient Electrocatalysts for the Oxygen Evolution Reaction: Insights into the Active Centers. *Nano Energy* **2017**, *41*, 417−425.
(43) Yin, J.; Li, Y.; Lv, F.; Lu, M.; Sun, K.; Wang, W.; Wang, L.; Cheng, F.; Li, Y.; Xi, P.; Guo, S. Oxygen Vacancies Dominated NiS_2/CoS_2 Interface Porous Nanowires for Portable Zn−Air Batteries Driven Water Splitting Devices. *Adv. Mater.* **2017**, *29*, 1704681.

https://dx.doi.org/10.1021/acscatal.9b05170
ACS Catal. 2020, 10, 1855−1864